

#### **PAPER • OPEN ACCESS**

# Reduction of thermal conductivity by nanopillar inclusion in thermoelectric vertically aligned nanocomposites

To cite this article: Marijn W van de Putte et al 2025 J. Phys. Energy 7 035009

View the <u>article online</u> for updates and enhancements.

# You may also like

- 2024 roadmap for sustainable batteries Magda Titirici, Patrik Johansson, Maria Crespo Ribadeneyra et al.
- Electronic structure and defect states in bismuth and antimony sulphides identified by energy-resolved electrochemical impedance spectroscopy Daria Miliaieva, Vojtech Nadazdy, Mykhailo Koltsov et al.
- Shape engineering and manufacturing of piezoceramics for energy conversion—a review

Guilherme Victor Selicani, Mahmoud Mobin, Vincenzo Esposito et al.

# Journal of Physics: Energy



#### **OPEN ACCESS**

#### RECEIVED

22 January 2025

#### REVISED

4 May 2025

ACCEPTED FOR PUBLICATION 12 May 2025

PUBLISHED

20 May 2025

Original content from this work may be used under the terms of the Creative Commons Attribution 4.0 licence.

Any further distribution of this work must maintain attribution to the author(s) and the title of the work, journal citation and DOI.



#### **PAPER**

# Reduction of thermal conductivity by nanopillar inclusion in thermoelectric vertically aligned nanocomposites

Marijn W van de Putte<sup>1</sup>, Jasman Singh Gambhir<sup>1</sup>, Nicolas Gauquelin<sup>2</sup>, Alexandros Sarantopoulos<sup>3</sup>, Daniel Monteiro Cunha<sup>1</sup>, Johan Verbeeck<sup>2</sup>, Gertjan Koster<sup>1</sup>, Francisco Rivadulla<sup>4</sup> and Mark Huijben<sup>1,\*</sup>

- $^1\,$  MESA+ Institute for Nanotechnology, University of Twente, PO Box 217, 7500 AE Enschede, The Netherlands
- <sup>2</sup> Electron Microscopy for Materials Science (EMAT), University of Antwerp, 2020 Antwerp, Belgium
- <sup>3</sup> Peter Grünberg Institute (PGI-7), Forschungszentrum Juelich GmbH and JARA-FIT, 52425 Jülich, Germany
- <sup>4</sup> Centro de Investigación en Química Biológica y Materiales Moleculares (CIQUS), Universidad de Santiago de Compostela, Santiago de Compostela, Spain
- \* Author to whom any correspondence should be addressed.

E-mail: m.huijben@utwente.nl

Keywords: thermal conductivity, thermoelectric, vertically aligned nanocomposite, nanopillar, epitaxy

#### **Abstract**

The phonon-glass electron-crystal paradigm has guided thermoelectric research in recent years. However, the inherent conflict between atomic disorder reducing phonon conduction, and the order required to maintain high electron mobility, creates a significant challenge in material design, which has driven innovation in nanostructuring and composite materials. Here, vertically aligned nanocomposites (VANs) composed of self-assembled metallic La<sub>0.7</sub>Sr<sub>0.3</sub>MnO<sub>3</sub> (LSMO) nanopillars in a surrounding ZnO matrix are investigated for controllable thermal conductivity. Tuning of the crystal orientation of the substrate controls the epitaxial alignment of the LSMO and ZnO phases along the horizontal and vertical interfaces. The VAN films on (111)-oriented STO substrates exhibit an increased power factor of 0.52  $\mu$ W·cm<sup>-1</sup>·K<sup>-2</sup> at 600 °C beyond ZnO films of 0.15  $\mu$ W·cm<sup>-1</sup>·K<sup>-2</sup>. Detailed characterization and modeling of the thermal conductivity demonstrates a reduction of about 75% as well as anisotropic behavior for the VAN films with out-of-plane and in-plane thermal conductivities of respectively 9.2 and 1.5 W·m<sup>-1</sup>·K<sup>-1</sup>, in strong contrast to the isotropic behavior in ZnO films with a thermal conductivity of 38 W·m<sup>-1</sup>·K<sup>-1</sup>. These results show the promising strategy of VAN thin films with a nanopillar-matrix architecture to scatter phonons and to enhance the thermoelectric performance.

#### 1. Introduction

The internet of things (IoTs) is a vast and quickly expanding network of smart devices, gadgets, and platforms, communicating with each other wirelessly and often autonomously. Data is gathered by sensors, processed on an internal chip, and sent wirelessly over a network to a central server from where it can be used to take action. Since all these steps require energy, typical IoT devices are fitted with a small battery. However, this results in several drawbacks such as the need for periodic replacement, fire hazard, environmental impact, and shipping restrictions of the involved batteries in those IoT devices. This could be overcome by replacing the battery with a local energy harvester; enabling the devices to harness energy from the local environment and to convert it into the required electrical energy. Several different energy sources are available for local harvesting depending on the environment of the IoT device: light, heat, radiofrequency waves and vibrations. The highest energy densities are present in light or heat, which can be converted by respectively solar panels and thermoelectric generators (TEGs). Inside buildings thermal energy is even the most promising candidate for energy harvesting enabling high power densities.[1]

TEGs directly convert thermal energy into electrical energy without moving parts, therefore exhibiting little degradation and long lifetimes which surpass typical lithium-ion batteries [2]. Significant research efforts are put into developing thermoelectric materials with a high figure of merit (ZT) by improving their

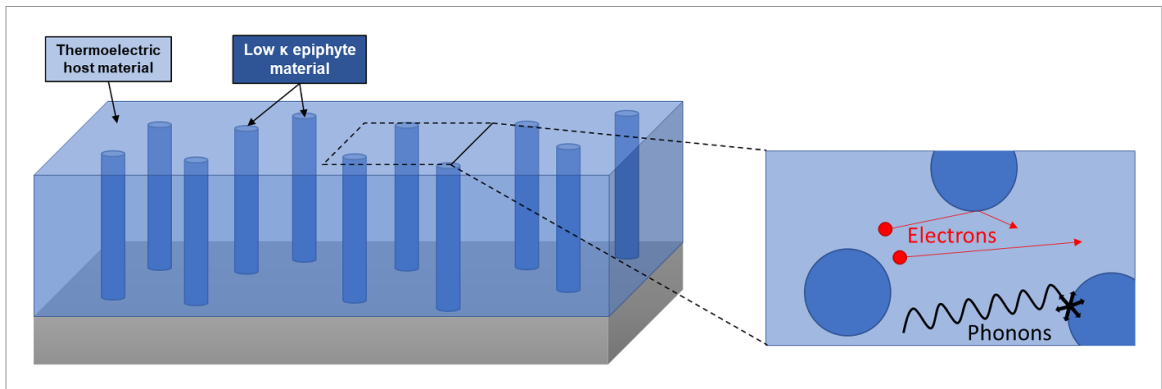


Figure 1. Schematic illustration of the VAN concept to impact the electrical and thermal transport in a thermoelectric material.

thermoelectric properties: Seebeck coefficient, electrical conductivity, and thermal conductivity [3–5]. However, it remains very challenging to optimize these parameters individually since they are all interrelated in a complex manner [6]. The ideal thermoelectric material is described as a 'Phonon glass electron crystal', an idealized material where electrons can easily travel as if it were a crystal, but where the phonons experience a disordered material similar to glass with lots of scattering [7, 8]. This will result in high electrical conductivity and Seebeck coefficient, but low thermal conductivity, and therefore, an optimized conversion efficiency.

There are three main strategies to increase the thermoelectric performance of materials, doping, nanostructuring or grain boundaries. Doping is the most widely used strategy as the electrical properties are easier to measure than the thermal properties, and therefore, is a more accessible approach in research. Doping is the introduction of foreign elements into a material to increase the charge carrier density, and the corresponding electrical conductivity. For example, doping a few percent of aluminum into insulating ZnO increases significantly the electrical conductivity. Although the Seebeck coefficient exhibits some decrease, the overall power factor is dramatically enhanced [9]. As a second strategy nanostructuring is applied for improving thermoelectric materials, ranging from nanoprecipitates [10] to superlattices [11], and nanowires [12]. Nanostructuring enhances the ZT of a material most often by influencing the phonon transport to reduce the thermal conductivity. The rule of thumb is that these nanostructures should be of similar length as the phonon mean free path to influence thermal transport [13]. A reduction of dimensions to the nanoscale can also increase the density of states significantly due to quantum confinement when the length scale approaches the mean free path of electrons, thereby increasing the Seebeck coefficient [14]. The third strategy is introducing grain boundaries into a material to improve thermoelectric properties by influencing the thermal conductivity. This can be done by switching from a single crystalline to a polycrystalline material. The added grain boundaries will scatter phonons to reduce thermal conductivity, but might also influence the electrical properties negatively by reducing the electrical transport due to the increased scattering of charge carriers. This can be seen in bulk thermoelectric materials, where polycrystalline materials exhibit typically lower performance as their single-crystalline counterparts [15]. Interestingly, all three strategies can also be combined, as was demonstrated for PbTe thermoelectric materials exhibiting the combination of Na doping, SrTe nano-inclusions and polycrystalline grains [16].

One innovative way to efficiently introduce nanostructures is through the self-assembly of a vertically aligned nanocomposite (VAN) architecture, which can be formed from two immiscible oxides and can exhibit specific properties not available in single-phase materials [17, 18]. These are composites consisting of two materials that self-assemble into a nanopillar-matrix structure with many vertical interfaces, which seems promising to scatter phonons and to improve the thermoelectric performance of a material. To study for the first time the concept of a VAN architecture to enhance the thermoelectric properties, a model system is required in which one material functions as thermoelectric host material that will form the matrix, while the other material should act as epiphyte material and form the nanopillars that scatter the phonons (figure 1). Previous studies have shown that VANs typically consist of a combination of two oxide materials with a dissimilar crystal structure, such as perovskite—wurtzite or spinel—perovskite [19, 20]. To observe the impact of introducing nanopillars onto the enhanced scattering of phonons, the chosen matrix material should exhibit a high thermal conductivity in bulk while the inclusion of a nanopillar material should enhance the phonon scattering and reduce the thermal conductivity.

Here, VANs composed of La<sub>0.7</sub>Sr<sub>0.3</sub>MnO<sub>3</sub> (LSMO) nanopillars in a surrounding ZnO matrix are investigated for the first time for a controllable thermal conductivity. VANs composed of LSMO and ZnO have previously been studied for their low-field magnetoresistance [21–25] in which ZnO nanopillars are

introduced in the LSMO film matrix. More recently, we have demonstrated the role of introducing LSMO nanopillars in the ZnO film matrix to influence the magnetic anisotropy [26]. ZnO is an interesting material for thermoelectric applications, as its properties can be influenced by doping [9, 27]. Although the high thermal conductivity in bulk ZnO of 49  $W \cdot m^{-1} \cdot K^{-1}$  [9] at 300 K normally poses a major problem for thermoelectric performance, it is the ideal material for our model system. It was shown previously that thermal conductivity in ZnO was based on phonons with mean free path in the range between 10 nm and  $2 \mu m$ , in which phonons in the 100–200 nm range cover about one third [9]. Furthermore, LSMO exhibits a much lower thermal conductivity in bulk of 2.8 W·m<sup>-1</sup>·K<sup>-1</sup> [28] and is therefore a good candidate to form the epiphyte nanopillars. In this study it is shown that highly ordered, crystalline LSMO:ZnO VAN films can be realized through self-assembly in which the achieved nanopillar-matrix architecture depends on the specific epitaxial relation to the underlying substrate  $SrTiO_3$  substrate, being either (100), (110), or (111)-oriented out-of-plane. Tuning of the crystal orientation of the perovskite SrTiO<sub>3</sub> substrate controls the epitaxial alignment of the pseudo-cubic perovskite LSMO and hexagonal wurtzite ZnO phases along the horizontal and vertical interfaces. The VAN films on (111)-oriented STO substrates exhibit a high Seebeck coefficient at 600 °C of about 980  $\mu$ V·K<sup>-1</sup>, comparable to N-doped ZnO, in combination with an enhanced electrical conductivity by a factor of 3 due to the inclusion of LSMO nanopillars. This results in an increased power factor of 0.52  $\mu$ W·cm<sup>-1</sup>·K<sup>-2</sup> at 600 °C for the VAN film beyond the result for ZnO films of  $0.15 \ \mu \text{W} \cdot \text{cm}^{-1} \cdot \text{K}^{-2}$ . Detailed characterization and modeling of the thermal conductivity demonstrates a reduction of about 75% as well as anisotropic behavior for the VAN films with out-of-plane and in-plane thermal conductivities of respectively 9.2 and 1.5 W·m<sup>-1</sup>·K<sup>-1</sup>, in strong contrast to the isotropic behavior in ZnO films with a thermal conductivity of 38 W·m<sup>-1</sup>·K<sup>-1</sup>. These results show the promising strategy of VAN thin films with a nanopillar-matrix architecture to scatter phonons and to enhance the thermoelectric performance.

# 2. Experimental

VAN thin films with ratio of (LSMO)<sub>0.1</sub>(ZnO)<sub>0.9</sub> were grown by pulsed laser deposition on SrTiO<sub>3</sub> (STO) substrates with different orientations (100, 110, 111). For comparison also pure La<sub>0.7</sub>Sr<sub>0.3</sub>MnO<sub>3</sub> (LSMO) films and pure ZnO films were grown by using stoichiometric targets. An oxygen pressure of 0.27 mbar was used for a growth temperature of 850 °C. A laser frequency of 5 Hz was used for the (LSMO)<sub>0.1</sub> (ZnO)<sub>0.9</sub> thin films (250 nm thickness) to achieve the self-assembled VAN formation [26], while 1 Hz was used for the pure LSMO (100 nm) and ZnO (200 nm) thin films to ensure high quality [29]. The surface morphology, crystal structure, composition, and thin film thickness were investigated by respectively atomic force microscopy (AFM, Bruker ICON Dimension Microscope), x-ray diffraction (XRD, PANalytical X'Pert PRO), and scanning electron microscopy (SEM, Zeiss Merlin). High-angle annular dark-field scanning transmission electron microscopy (STEM) and energy dispersive x-ray spectroscopy (EDX) were performed on a FEI Titan 80–300 aberration corrected electron microscope operated at 300 kV, equipped with a Super-X EDX detector, to study the structural and compositional properties in more detail. The cross-section STEM lamellas were prepared using a FEI Helios 650 dual-beam focused ion beam. The temperature dependent electrical transport properties were characterized for temperature range 10-300 K by using a Dynacool PPMS system (Quantum Design), while a Linseis LSR-3 system was used for temperature range 300–900 K. The high-temperature thermoelectric properties of the VAN films were determined with a rate of 3 °C min<sup>-1</sup> during heating and cooling. To exclude the effect of possible thermal degradation, films are cycled consecutively from room temperature to a target temperature and back to room temperature (i.e. RT-100 °C-RT, RT-200 °C-RT, ..., RT-600 °C-RT) to confirm the absence of irreversible changes in the materials. A gas mixture of 1.0 bar helium and 0.1 bar oxygen was used as a successful method to prevent irreversible oxygen vacancy formation in oxide thin films up to 600 °C [30].

The thermal conductivity was measured by frequency-domain thermoreflectance (FDTR) measurements using the method as described in [31] of a previous study. FDTR is a non-contact optical pump—probe technique, in which one beam of light (the pump) acts as a heat source while a second beam (the probe) detects the resulting temperature change through a change in surface reflectivity The samples were coated with a 60 nm gold layer to act as a heat transducer. The intensity of the pump laser,  $\lambda=405$  nm, was modulated from 2 kHz to 50 MHz, and the periodic variation of the Au thermoreflectance was probed at  $\lambda=532$  nm. The probe beam is split before reaching the sample to work as a reference signal, improving the signal-to-noise ratio at low frequencies and compensating phase-shift offsets from beam paths and electronics.

The thermal properties of the sample were determined through multi-parameter fitting of the phase lag of the pump/probe lasers,  $\phi(\omega)$ , as explained in [32]. The different parameters of the model were measured independently or obtained from the literature, so that  $\kappa$  of the film is the only fitting parameter. For instance,

Table 1. Parameters used in the fitting of FDTR data for all components present in the thin films.

	LSMO	ZnO	$(LSMO)_{0.1}(ZnO)_{0.9}$	STO
Density $(g \cdot cm^{-3})$	6.45 [34]	5.61 [35]	5.79	5.12 [36]
Cp $(J \cdot mol^{-1} \cdot K^{-1})$	128.6 [37]	40.3 [35]	49.1	99.1 [38]

the thermal conductivity of the SrTiO<sub>3</sub> substrates was derived from Langenberg *et al* [33]; for Au we measured the electrical conductivity in co-deposited samples and applied the Wiedemann–Frantz law to determine its thermal conductivity. The Cp of the SrTiO<sub>3</sub> substrate (see table 1) and Au transducer (Cp = 25.4 J·mol<sup>-1</sup>·K<sup>-1</sup>) were derived from previous studies. The thickness of the Au transducer layer was determined by x-ray reflectivity and was kept fixed in all the experiments. Finally, two different spot sizes, Gaussian  $1/e^2$  radius  $\approx 3.7$  or  $10.5 \,\mu$ m, were used to increase the sensitivity to the in-plane/out-of-plane thermal conductivity.

#### 3. Results and discussion

#### 3.1. Structural properties

To investigate if the host—epiphyte phase formation of a LSMO:ZnO nanocomposite can be affected by using a different substrate orientation, VANs have been grown on STO (100), (110), and (111)-oriented substrates. Since the pseudo-cubic perovskite LSMO phase (lattice parameter a=3.889 Å [39]) is structurally close to the cubic perovskite STO substrate (a=3.905 Å [36]), it is expected that the LSMO matches the substrate better than the hexagonal wurtzite ZnO phase for all orientations and, therefore, will always form the matrix. This would naturally result in LSMO interface layers on all samples if surface diffusion is high enough. However, the exposed surfaces of the differently oriented STO substrates could exhibit variations in activation energies for surface diffusion of different materials. To predict the expected orientations of the crystal structures for both LSMO and ZnO phases within the VAN films, the lattice matching with the substrate is considered.

In figure 2 the top view schematics are shown for the STO, LSMO, and ZnO unit cells and their possible orientations with respect to each other and the corresponding lattice mismatches. Only the horizontal interfaces with the substrates are considered here, while the vertical interfaces between the LSMO and ZnO phases are not taken into account. On a STO (100) substrate the LSMO phase fits best if it grows cube on cube, while the ZnO phase matches best in the (1120) orientation although with some significant strain. On a STO (110) substrate the LSMO phase grows in the same (110) out-of-plane orientation, however, the ZnO phase now fits best if it grows in the (0001) orientation. Even though it has only a small mismatch of only 1.9% in one direction, the other direction has a very large mismatch of more than 17%. On a STO (111) substrate the LSMO is again predicted to grow in the same (111) orientation as the substrate, while the ZnO is again growing in the (0001) orientation with an in-plane strain of 4.1%. These predictions are based solely on lattice matching with the substrate. As is known, in VANs the vertical interfaces are very important and dominate the strain states and crystal phases of materials. Therefore, the actual orientations in the nanocomposites could differ from these predictions if the vertical interfaces created by these predicted orientations are energetically very unfavorable.

The surface morphology and internal nanostructures of the VAN films grown on differently oriented STO substrates are characterized by SEM and AFM analysis (figure 3). The SEM cross-sectional images reveal the dark LSMO nanopillars within a bright ZnO matrix. A clear separation of the LSMO and ZnO phases was previously confirmed by STEM-EDX analysis for the VAN film grown on (100)-oriented STO substrates [26]. The rms roughness of the VAN films is very similar for all nanocomposites grown on STO (100), (110), and (111) substrates with values of 7 nm, 6 nm, and 3 nm respectively.

A structural characterization of the VANs grown on different STO substrates has been performed and the corresponding goniometric and phi scans are shown in figure 4. As described above, the ZnO and LSMO phases in the nanocomposite grown on a STO (100) substrate are oriented respectively in the ( $11\bar{2}0$ ) and (100) directions (figure 4(a)), as was demonstrated previously [17, 26]. The in-plane symmetry indicates that the LSMO phase grows in the same orientation (in-plane and out-of-plane) as the STO (100) substrate (figure 4(d)), while the ZnO phase is 45° rotated in-plane as compared to the principal axes of the STO structure. In figure 4(g) a schematic representation of the unit cells is shown indicating their match to the substrate, which is in good agreement with literature [24].

The VAN film grown on a STO (110) substrate shows a single (0001) out-of-plane orientation for the ZnO phase (figure 4(b)). The LSMO phase shows up in the tail of the STO peaks on the right side, indicating growth in the (110) orientation. The in-plane orientation of the phases is shown in figure 4(e) and indicates

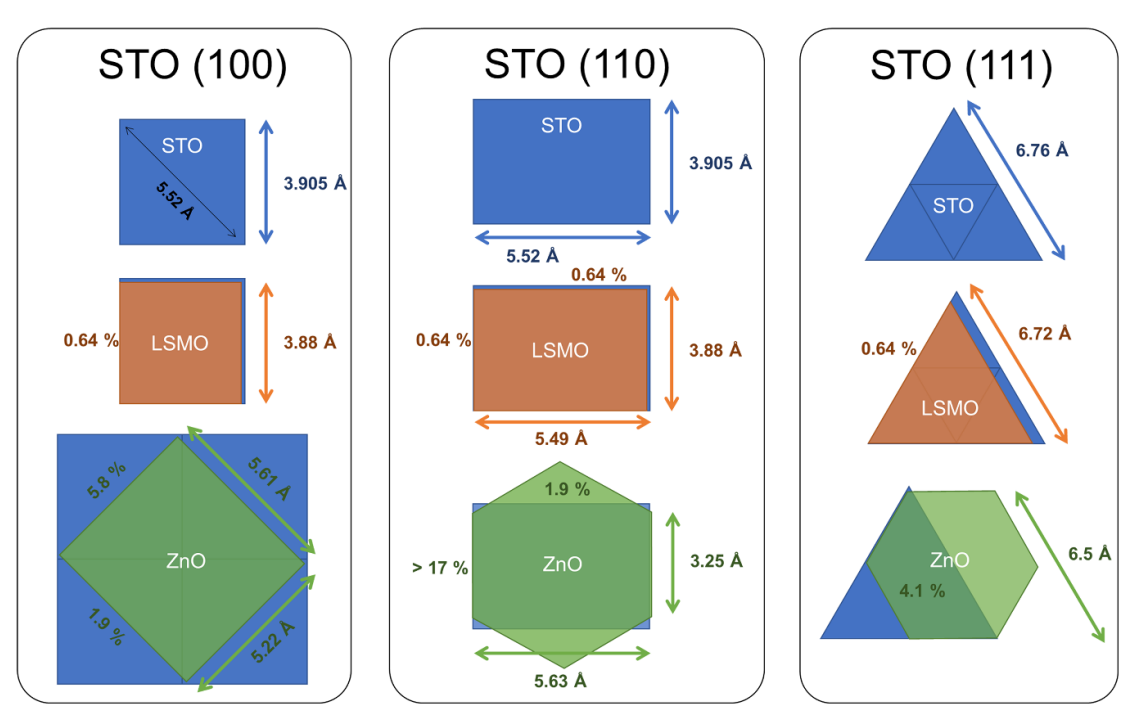


**Figure 2.** Schematic view of the lattice matching of the ZnO and LSMO phases on different STO substrate orientations, with lattice parameters and epitaxial mismatch.

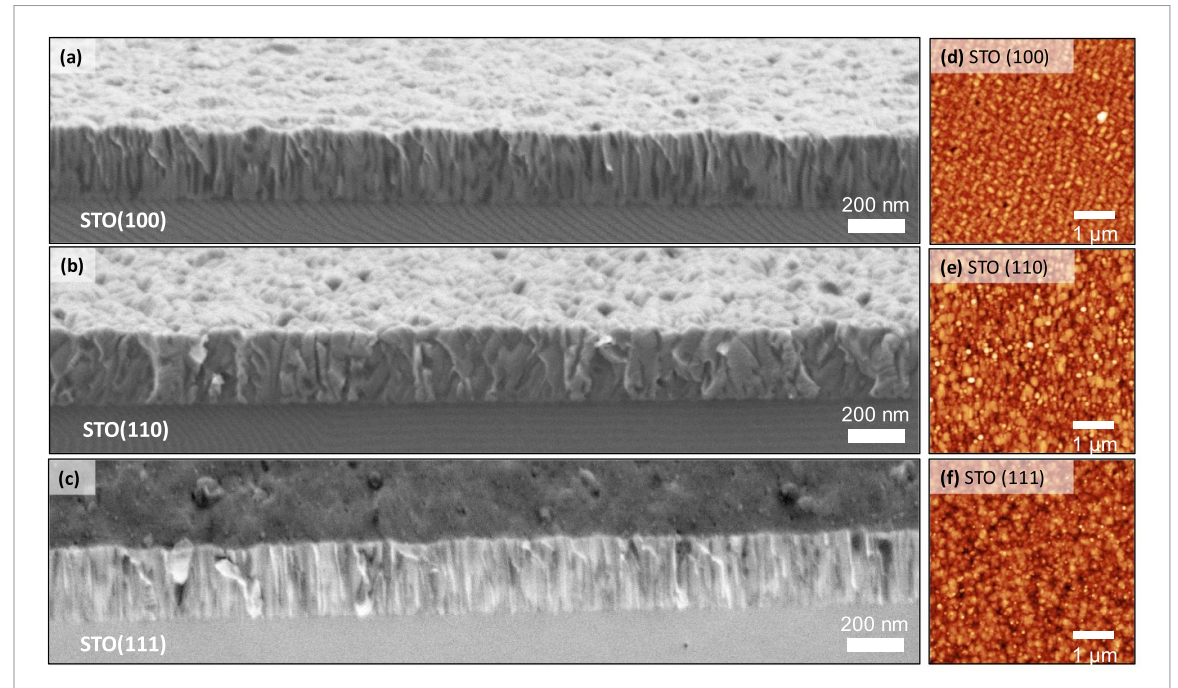
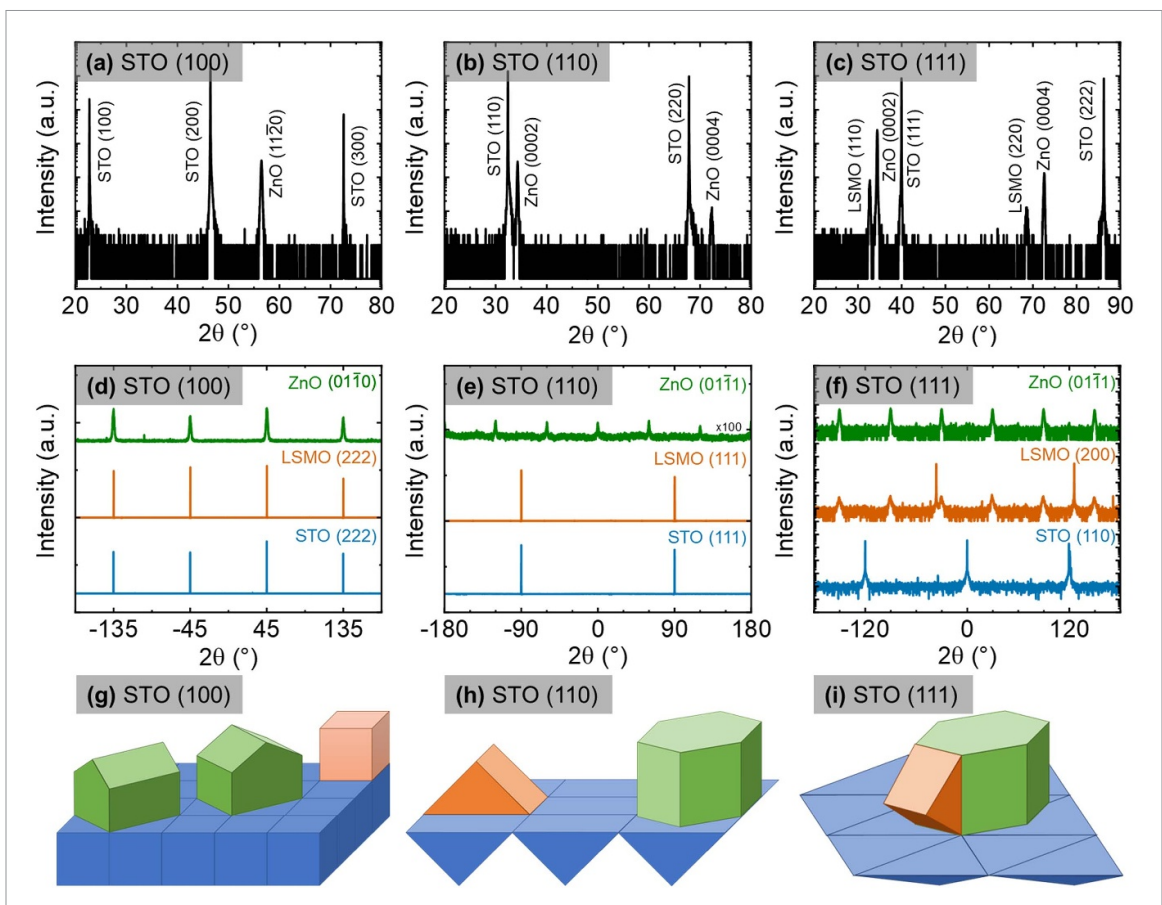


Figure 3. (a)–(c) Cross-section SEM images of the  $(LSMO)_{0.1}(ZnO)_{0.9}$  nanocomposites grown on STO (100), (110), and (111) substrates, respectively. (d)–(f) AFM images showing the surface morphology the nanocomposites grown on STO (100), (110), and (111) substrates, respectively.

a twofold symmetry for both the STO substrate and the LSMO phase, which confirms that the LSMO grows in the same orientation (in-plane and out-of-plane) as the substrate. The ZnO  $(01\bar{1}1)$  peaks show a sixfold in-plane symmetry with an offset of 30° from the STO (111) peaks indicating that the ZnO phase grows as indicated in the schematic in figure 4(h). The epitaxial relations are determined to be

$$\begin{split} &(0001)_{ZnO} /\!/(110)_{STO} /\!/(110)_{LSMO} \\ &(\bar{1}100)_{ZnO} /\!/(1\bar{1}0)_{STO} /\!/(1\bar{1}0)_{LSMO}. \\ &(11\bar{2}0)_{ZnO} /\!/(001)_{STO} /\!/(001)_{LSMO}. \end{split}$$



**Figure 4.** Comparison of goniometric XRD scans of vertically aligned nanocomposites grown on (a) STO (100), (b) STO (110), and (c) STO (111) substrates. Phi scans of nanocomposites grown on (d) STO (100), (e) STO (110), and (f) STO (111) substrates. (g)–(i) Schematic representations of the crystal orientations of the LSMO (orange) and ZnO (green) phases within the nanocomposites on the differently oriented STO (blue) substrates.

The goniometric scan of the VAN film grown on the STO (111) substrate in figure 4(c) shows the ZnO phase grown in the (0001) orientation out-of-plane and the LSMO phase grown in the (110) direction. Interestingly, the LSMO phase does not follow the same orientation as the STO substrate, in contrast to the other two cases for VAN films grown on (100)- and (110)-oriented STO substrates, indicating that the epitaxial relationship is determined more strongly by the internal vertical interfaces in the nanocomposite itself rather than the horizontal substrate interface. In the phi scans shown in figure 4(f) the in-plane relation of the nanocomposite is determined. The STO substrate shows a threefold symmetry of the (110) peak, while the ZnO (01 $\bar{1}1$ ) peaks exhibit a sixfold symmetry with a 30° offset. The LSMO (200) peaks show the same sixfold symmetry as the ZnO at the same phi angles which confirms that the orientation of the LSMO phase is indeed dependent on the ZnO phase. The orientations of the phase are illustrated in figure 4(i). The epitaxial relations are determined to be

$$(0001)_{Z_{\text{RO}}} / (111)_{S_{\text{TO}}} / (110)_{LSMO}$$
  
 $(\bar{1}100)_{Z_{\text{RO}}} / (1\bar{1}0)_{S_{\text{TO}}} / (1\bar{1}0)_{LSMO}$   
 $(11\bar{2}0)_{Z_{\text{RO}}} / (11\bar{2})_{S_{\text{TO}}} / (001)_{LSMO}$ 

When comparing the epitaxial relations of all three VAN films, the epitaxial alignment of the LSMO and the ZnO crystal structures is always equal, suggesting that these internal interfaces in the nanocomposites are energetically the most favorable to create.

### 3.2. Nanopillar-matrix structure alignment

To evaluate the nanostructures in more detail, STEM analysis was performed on lamella cut along the STO  $(1\bar{1}0)$  direction for the VAN film grown on a STO (111) substrate. The thickness of the STEM lamella is about 10 nm, which results in overlap regions where both LSMO and ZnO phases seem to be present. The width of the LSMO pillars in this  $(LSMO)_{0.1}(ZnO)_{0.9}$  VAN thin film on (111)-oriented STO substrate is estimated to be between 10 and 30 nm, similar to nanopillar dimensions of  $(LSMO)_{0.1}(ZnO)_{0.9}$  VAN thin

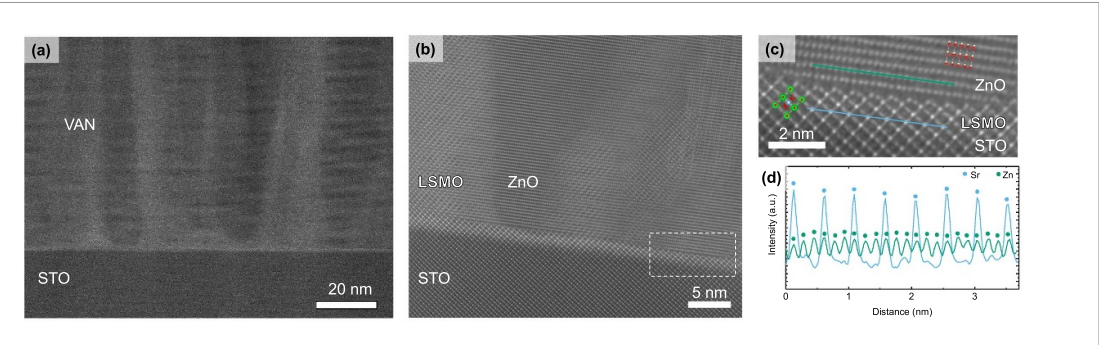


**Figure 5.** Scanning transmission electron microscopy images of the (a) VAN film grown on a STO (111) substrate, (b), (c) zoom-in of the substrate-VAN interface. (c) Intensity profiles of the substrate and ZnO phases taken along the colored lines in figure c.

film on (001)-oriented STO substrate [26]. A bright interface layer can be seen at the VAN-substrate interface, see figure 5. Since the contrast is given by the atomic number, where heavier elements are brighter than the lighter atoms, the interface layer most likely consists of La atoms. This layer is only a few atomic layers thin, and its structure exhibits the same perovskite structure as the underlying STO substrate, suggesting the formation of an LSMO interface layer. No significant crystallographic defects can be observed for both phases of the VAN composite, suggesting a good lattice matching between them. The ZnO and LSMO phases seem to separate well, although, some areas exist where the two crystal structures overlap.

Detailed analysis of the horizontal interface between the STO substrate and the VAN film indicates periodic matching between the Zn atoms and the Sr atoms (figure 5(b)). The intensity profiles of both ZnO and LSMO/STO phases are shown figure 5(d), where every third ZnO atom matches its position with a Sr atom. The intensity profiles are not taken directly at the interface to obtain the general relation between the two crystal structures without interference from the interface. The first row of Zn atoms at the interface are distorted from their bulk positions, as the distance between them is not equal everywhere, which is likely caused by the hexagonal wurtzite phase adapting to the perovskite phase of the substrate/interface layer. The interlayer distance at the interface is close to the distance between Zn atoms along the *c*-axis, suggesting that the ZnO phase starts with an oxygen layer, bonded to the underlying perovskite LSMO phase. The top (La/Sr)O layer of the perovskite LSMO phase at the interface seems to be distorted to enable the lattice matching to the hexagonal wurtzite ZnO phase.

When characterizing the vertical interfaces in the VAN film close to the underlying STO substrate, LSMO phase is continued growing in the (111) out-of-plane direction while the ZnO grows in the (0001) orientation (figure 6). However, XRD analysis indicated growth of the LSMO phase in the VAN film on STO (111) substrates primarily along the (110) orientation (figure 4(c)). Interestingly, in the first stages of VAN growth, there are only a limited number of vertical interfaces between the LSMO and ZnO phases, and therefore the perovskite LSMO phase aligns with the perovskite STO substrate. A similar effect has been observed in SmO:BiFeO<sub>3</sub> VANs, where in the initial 20 nm the strain state is dictated by the substrate, whereas for thicker layers the vertical interfaces determine the strain state [17]. Here, it is not the strain state that is affected, but the crystallographic orientation of the LSMO phase. Furthermore, due to the thickness of the lamella the overlapping LSMO and ZnO phases show an interesting moiré-like interference pattern, as indicated by the white arrows in figure 6(a). Every 8 atomic planes of ZnO, the atomic plane lines up with the LSMO phase, exhibiting 9 atomic planes for the same length (figure 6(b)). The intensity profiles for the ZnO and LSMO phases are shown in figure 6(c) and by overlapping the out-of-plane distances an 8:9 ratio in atomic planes is confirmed. Epitaxial alignment of the bulk ZnO ( $d_{ZnO} = 7 * \frac{c}{2} = 18.26$ Å) and LSMO  $(d_{\rm LSMO} = 8 * \frac{\sqrt{3}}{3} a = 17.92 \text{Å})$  crystal lattices would lead to a theoretical mismatch of 1.9%. As the ZnO phase dominates the VAN composition, an induced out-of-plane tensile strain is expected for the LSMO phase, leading to a theoretical elongation of the structure in the (111) direction from the bulk 2.24 Å to 2.28 Å. At the horizontal interface between the perovskite STO substrate and the perovskite LSMO phase an epitaxial alignment occurs, as discussed above. However, further away from the STO substrate the LSMO phase is influenced mainly by the vertical interfaces with the ZnO phase and experiences no significant influence from the substrate. In figures 7(a) and (b) can be seen that the LSMO phase is oriented out-of-plane in the (110) orientation, as evidenced by the 45° rotated cubic perovskite unit cell, while the ZnO phase is still oriented out-of-plane in the (0001) direction. Although the sharp vertical interface suggests a 1:1 lattice matching between the LSMO and ZnO phases along the out-of-plane direction, the measured out-of-plane lattice parameters from the XRD analysis (figure 4(c)) of 2.609 Å and 2.733 Å for ZnO and LSMO

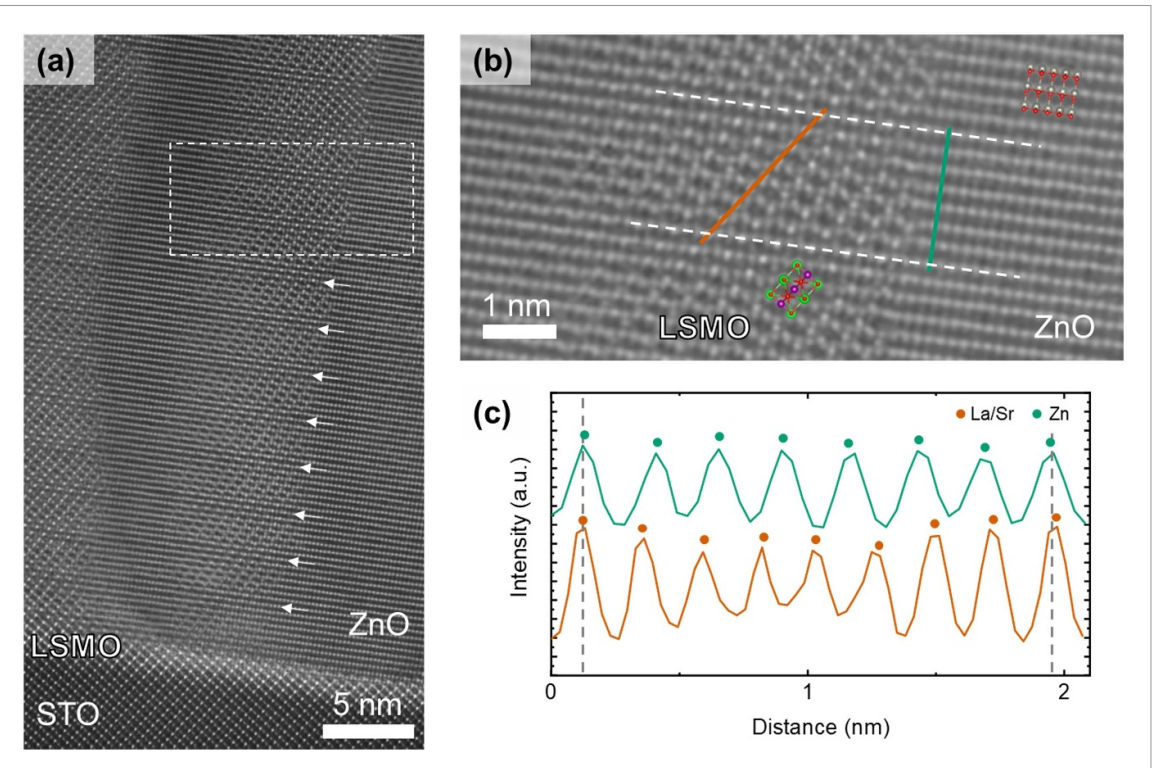


**Figure 6.** Scanning transmission electron microscopy images of the (a) VAN film grown on an STO (111) substrate, (b) zoom-in of the overlapping ZnO and LSMO phases. (c) Intensity profiles of the LSMO and ZnO phases taken along the colored lines in figure b.

respectively, indicate a lattice mismatch of almost 5%. To determine the presence of possible domain matching along this orientation, the intensity profiles of the LSMO and ZnO phases are overlapped in figure 7(c), which reveals a domain matching of 22 atomic planes of LSMO with 23 planes of ZnO. This corresponds to a unit cell ratio of 21:22 unit cells for LSMO(110):ZnO(0001) with a low mismatch of only 0.008%. Previous study of  $(LSMO)_{0.1}(ZnO)_{0.9}$  VAN films grown on STO (100) substrates showed domain matching of 5:6 unit cells for LSMO(100):ZnO(11–20) [17, 26]. An illustrative schematic of the domain matching in these LSMO:ZnO VAN films is shown in figure 7(d).

#### 3.3. Electrical properties

To determine the influence of the substrate crystal orientation on the resistivity of the different VAN films, temperature dependent measurements were performed using the van der Pauw geometry (figure 8). As shown previously, the LSMO:ZnO VAN film on a STO (100) substrate shows a metallic-like temperature dependence of the resistivity  $(d\rho/dT > 0)$  behavior below room temperature [26]. However, for temperatures above 320 K the resistivity values become constant and even decrease slightly above the metal–semiconductor ( $d\rho/dT < 0$ ) transition. In contrast, the VAN film grown on a STO (110) substrate exhibits much higher resistivity values over the full temperature range with a clear semi-conducting behavior. There is still a metal-to-insulator transition visible around 200 K, indicating that an electronic percolation path still exists through the LSMO phase, which becomes more dominant at lower temperatures. Finally, the VAN film grown on a STO (111) substrate exhibits even higher resistivity values reaching the limit of the equipment. Interestingly, the LSMO interface layer of a few atomic layers at the STO substrate surface does not play a significant role in the electrical transport. It has previously been demonstrated that a critical thickness exists of a few unit cells for a LSMO layer to exhibit conducting behavior [29]. Strain can cause the differences in electrical properties between the VAN films on substrates with different crystal orientations, as it is known that large amounts of strain can drastically change the transport behavior of LSMO from metallic to semi-conductive [40]. Not only do the different VAN films consist of nanocomposites with different strain states of the LSMO phase after thin film growth, as discussed above, the different thermal expansion coefficients (1.5  $\times$  10<sup>-5</sup> K<sup>-1</sup> for ZnO [41] and 1.34  $\times$  10<sup>-5</sup> K<sup>-1</sup> for LSMO [42]), can affect the strain even further upon cooling down below room temperature.

To study the differences in thermoelectric properties of the VAN films as compared to pure ZnO or LSMO thin films, the resistivity and Seebeck coefficient values were simultaneously measured (figure 9). The differences in resistivity for the VAN films on differently oriented STO substrates are gradually reduced when

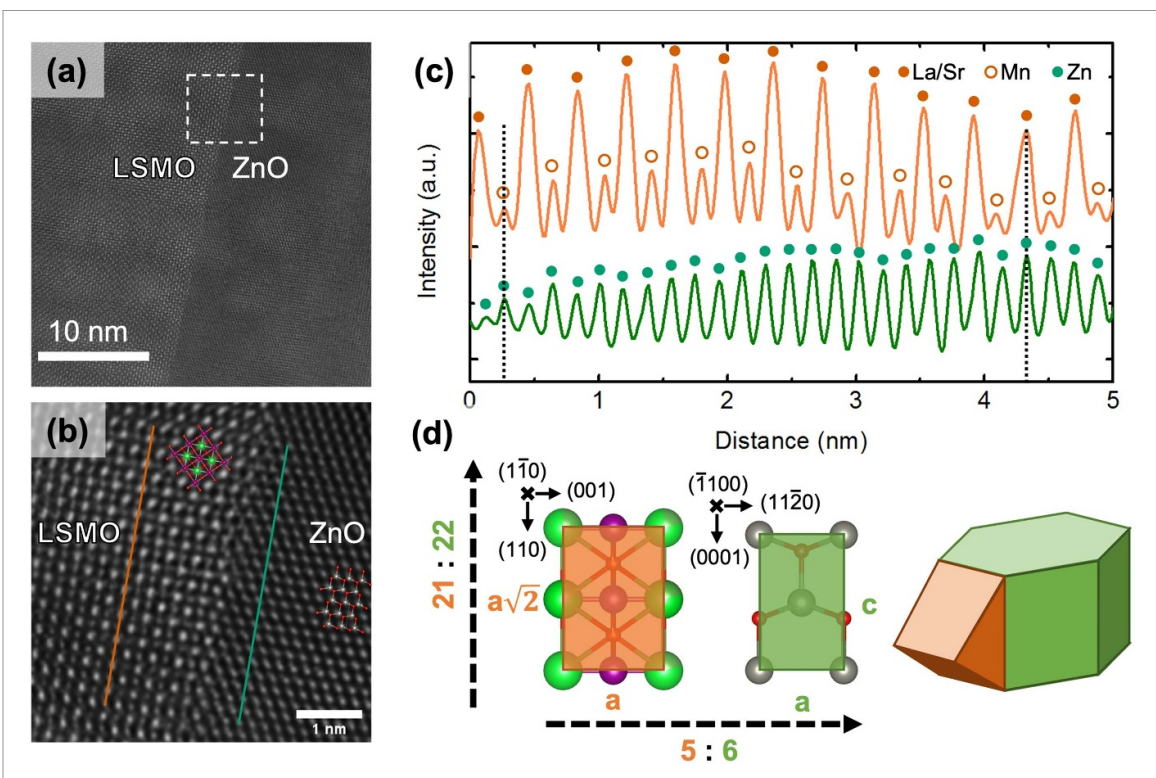


**Figure 7.** Scanning transmission electron microscopy images of the (a) vertical interface between the LSMO and ZnO in the bulk of the nanocomposite, (b) zoom-in of the vertical interface. (c) Intensity profiles of the LSMO and ZnO phases taken along the colored lines in figure b. (d) Illustrative schematic of domain matching in LSMO:ZnO VAN films.

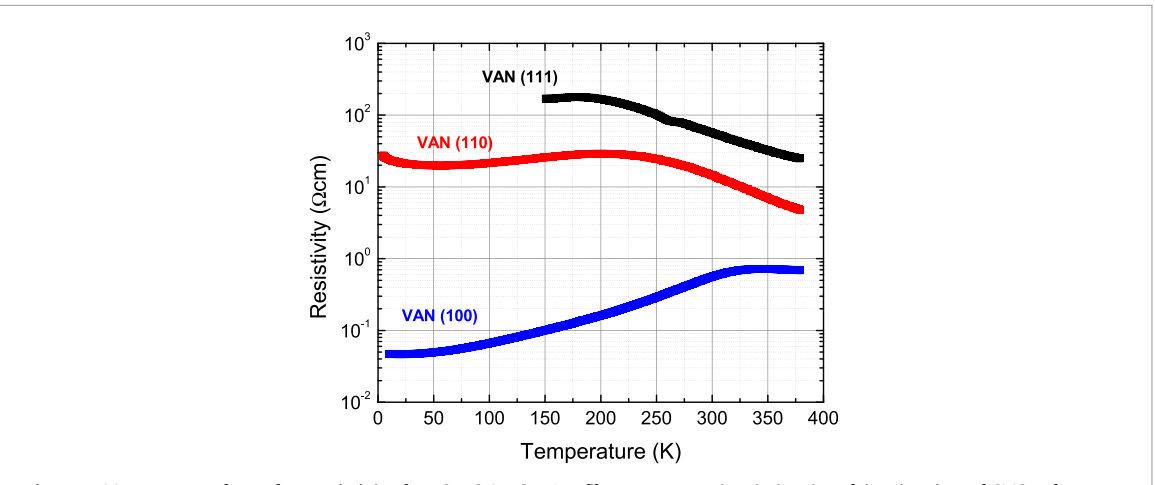
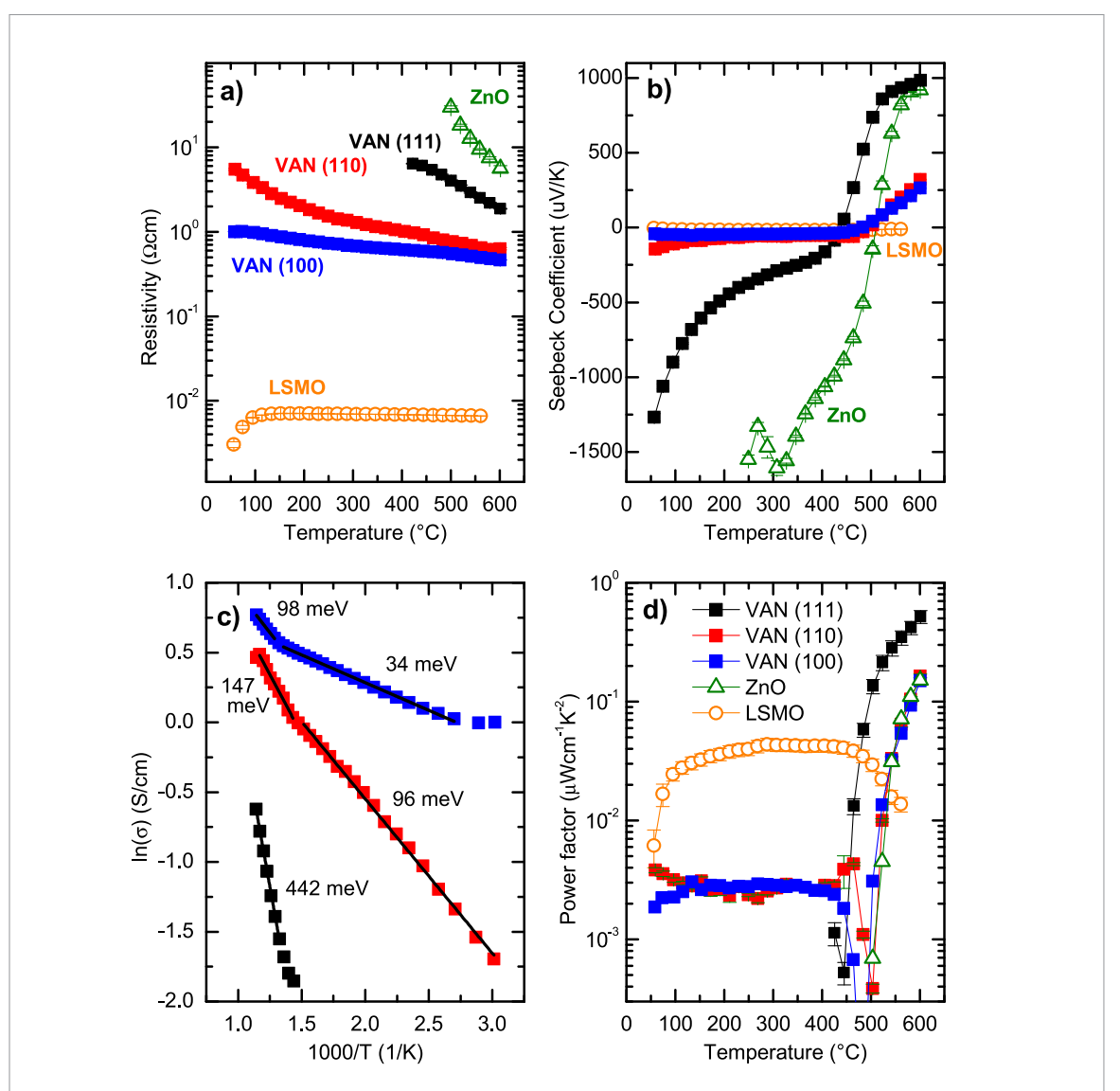


Figure 8. Temperature dependent resistivity for LSMO:ZnO VAN films grown on (100), (110) and (111)-oriented STO substrates.

temperatures increase from room temperature upto 600 °C. All three samples exhibit semiconducting behavior with a decreasing resistance with increasing temperature. The resistivity values of the phase pure LSMO (100 nm) and ZnO (200 nm) reference films on STO (100) substrates are shown for comparison. The LSMO thin film shows a near-constant resistivity above the metal–insulator transition, in good agreement with previous study [43]. The ZnO thin film exhibits a much higher resistivity, which is known to dependent highly on the presence of native defects [44]. The temperature dependent Seebeck coefficient values are shown in figure 9(b). The VAN films on STO (100) and STO (110) substrates show very similar behavior, while the VAN film on the STO (111) substrate shows an order of magnitude higher absolute Seebeck coefficients at room temperature. This is the typical charge carrier dependent inverse relation between (low) electrical conductivity and (high) Seebeck coefficient. At 600 °C the VAN films on STO (100) and STO (110) substrates exhibit Seebeck coefficient values of respectively 260 and 320  $\mu$ V·K<sup>-1</sup>. However, the VAN films on STO (111) substrates achieve values of about 980  $\mu$ V·K<sup>-1</sup> very close to the results for ZnO films, in good agreement with DFT calculations for N-doped ZnO [45].



**Figure 9.** Temperature dependent (a) resistivity and (b) Seebeck coefficient of LSMO:ZnO VAN films grown on (100), (110) and (111)-oriented STO substrates (resp. blue, red and black squares), as well as LSMO and ZnO thin films grown on (100)-oriented STO substrates (resp. orange circles and green triangles). (c) Arrhenius plot of conductivity behavior of VAN films in (a). Temperature dependent power factor of VAN films as well as LSMO and ZnO films.

Interestingly, a transition from n-type to p-type charge carrier behavior can be observed for all VAN films at 481 °C, 496 °C and 437 °C for respectively STO (100), STO (110) and STO (111) substrates. This transition is absent for a phase pure LSMO film for which the Seebeck coefficient remains negative between -4 and  $-18~\mu\text{V}\cdot\text{K}^{-1}$ , in good agreement with literature [46, 47]. Also previous studies by us on the same LSR-3 system did not exhibit such transition at elevated temperatures, for example phase pure  $\text{Ca}_3\text{Co}_4\text{O}_9$  [30] or SnSe films [48]. It also indicates that the used STO substrate and the measurement setup are not the origin for the observed n-p transition in the VAN films. However, the temperature dependent Seebeck coefficient of a phase pure ZnO film exhibits a very similar n-p transition at 510 °C indicating a change in the electronic structure. Interestingly, the opposite p-type to n-type transition is typically observed with increasing temperature for some materials in previous studies. For example, a semiconductor to metal transition in  $\text{Pb}_{1-x}\text{Eu}_x\text{Te}$  [49], selenium vacancy formation in  $\text{Cu}_{1+x}\text{FeSe}_2$  [50], or a structural transition in  $\text{CaMn}_{1-x}\text{Mo}_x\text{O}_3$  [51]. Such transition has not been reported yet for ZnO, but should be due to a change in the atomic or electronic structure.

Detailed temperature-dependent XRD analysis of the VAN film grown on a STO (100) substrate confirmed the expected thermal expansion of the ZnO and STO crystal structures, respectively 3.25596–3.26436 Å and 3.90462–3.92644 Å from 30 °C to 600 °C [52, 53]. The limited volume of the LSMO phase in the VAN film hampers detailed analysis of its crystal structure. However, the ZnO phase dominates the Seebeck coefficient behavior and does not exhibit a structural transition at such elevated temperatures. Furthermore, a change in electronic structure could be caused by thermally activated carriers. The observed

transition temperature of around 437 °C–510 °C, suggests an activation barrier of about 61–68 meV. It is known that relatively small concentrations of native point defects (i.e. vacancies, interstitials, and antisites) and impurities can significantly affect the electrical properties in ZnO [40]. Often unintentional n-type conductivity is observed at room temperature for as-grown ZnO crystals, and thought to be caused by oxygen vacancies and/or zinc interstitials. However, combined experimental and theoretical studies have led to the conclusion that it is the unintentional incorporation of impurities that act as shallow donors, such as hydrogen which is present in almost all growth and processing environments [44].

Here, the phase pure ZnO thin film exhibits very high resistivities at low temperature (figure 9(a)) suggesting the absence of significant number of impurities. For higher temperatures (250 °C–510 °C) n-type conductivity was determined, most likely caused by interstitial hydrogen acting as shallow donors with a reported ionization energy of about 35 meV [44, 54, 55]. However, the phase pure ZnO film exhibits a transition to p-type conductivity above 510 °C. Previous studies have indicated p-type conductivity in N-doped ZnO in which N substitutes for O and acts as a shallow acceptor with a reported ionization energy of about 100 meV [56-58]. For all VAN films a n-type to p-type transition was observed in the temperature range 437 °C–496 °C, which were fully reversible as confirmed by consecutive measurements over the same temperature range (not shown). To gain more insight into the behavior of the thermally activated carriers, an Arrhenius-type plot was made using the conductivity data of the three VAN films (figure 9(c)). There exist distinct slopes, indicating two different conduction mechanisms present in the VAN films. The calculated activation energies of 34 meV and 98 meV for the VAN film on STO (100) are in good agreement with previously reported values for respectively hydrogen and nitrogen doping, as discussed above. The VAN films on STO (110) and STO (111) exhibit higher activation energies most likely caused by the differences in nanopillar-matrix structures. Possible ionic conductivity of oxygen in ZnO can be excluded, as previous studies reported two orders of magnitude lower ionic conductivity values as compared to electronic conductivity for this temperature range [59].

The VAN films exhibit values for the achieved power factor of about  $3 \times 10^{-3}~\mu \text{W} \cdot \text{cm}^{-1} \cdot \text{K}^{-2}$  for temperatures between room temperature and 400 °C. The LSMO film provides a power factor of about  $4 \times 10^{-2}~\mu \text{W} \cdot \text{cm}^{-1} \cdot \text{K}^{-2}$  for the same temperature range, which is higher than previously observed of about  $7 \times 10^{-3}~\mu \text{W} \cdot \text{cm}^{-1} \cdot \text{K}^{-2}$  at 250 °C for mesoporous LSMO thin films [46, 47]. Above 400 °C the power factor for the LSMO thin film reduces, due to a decrease in Seebeck coefficient from -18 to  $-10~\mu \text{V} \cdot \text{K}^{-1}$ . However, the VAN films as well as the ZnO film exhibit above 400 °C a sharp increase in power factor of several orders of magnitude, caused by the dramatic change in Seebeck coefficient as discussed above. The VAN films on STO (100) and STO (110) substrates show very similar behavior to the ZnO film reaching a power factor of  $0.15~\mu \text{W} \cdot \text{cm}^{-1} \cdot \text{K}^{-2}$  at 600 °C. In contrast, the VAN film on the STO (111) substrate exhibits a power factor of  $0.52~\mu \text{W} \cdot \text{cm}^{-1} \cdot \text{K}^{-2}$  at 600 °C. In this specific VAN nano-architecture the high Seebeck coefficient typical for ZnO is combined with an enhanced electrical conductivity by a factor of 3 due to the inclusion of LSMO nanopillars.

#### 3.4. Thermal conductivity

The impact of the nanopillar-matrix architecture in the VAN films on the thermal conductivity was studied by FDTR. As explained before, the thermal properties of the sample were determined through multi-parameter fitting of the phase lag of the pump/probe lasers,  $\phi(\omega)$  [32]. For the different materials present in the VAN film samples (STO, LSMO, ZnO), the volumetric heat capacity was calculated using the density and molar heat capacity as determined in previous studies (table 1). For the  $(LSMO)_{0.1}(ZnO)_{0.9}$ nanocomposite films, the values were estimated based on the molar ratio of its components. The thickness of the films was determined by the number of laser pulses during the PLD growth process. For the interface thermal conductance between the film and the substrate, typical values of oxide-oxide interfaces  $(\approx 370(20) \text{ MW} \cdot \text{m}^{-2} \cdot \text{K}^{-1})$  were used. Given the relatively large thickness of the films, the sensitivity of the fitting to this parameter is small. Moreover, by measuring films with different thicknesses but with the same composition, any possible influence of the thermal conductance of the interface was minimized in the results. For the oxide–gold interfaces a value of  $\approx 70(15) \text{ MW} \cdot \text{m}^{-2} \cdot \text{K}^{-1}$  provided the best fitting of the data, and was used for all interfaces. This value is in the range expected for Au/oxide interfaces of the quality of our films [60]. Keeping all these parameters fixed and only fitting the thermal conductivity of the films increases the robustness of the extracted thermal conductivity parameters, and increases the sensitivity to the relative differences between the films.

The data measured for the ZnO thin film reference sample and the VAN films on STO (100) substrates with different thicknesses of 250 nm, 160 nm, and 80 nm are shown in figure 10(a). A sensitivity analysis showed that the high-frequency range between 100 kHz and 50 MHz has maximum sensitivity to the thermal conductivity. The VAN films exhibit a strongly reduced phase in the high-frequency range as compared to the ZnO thin film, which is characteristic of a large reduction in thermal conductivity. In figure 10(b) the

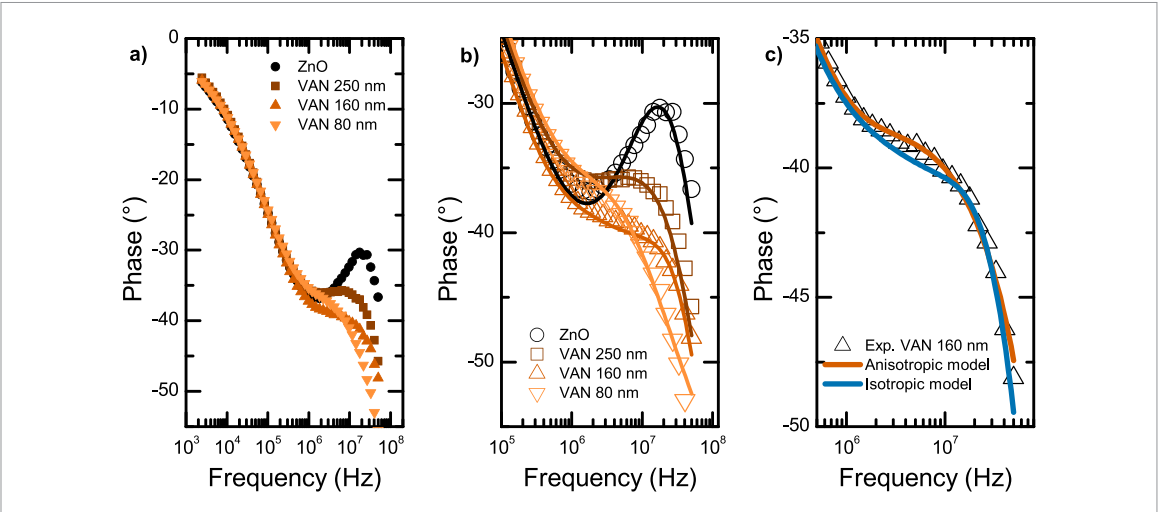


**Figure 10.** (a) FDTR results at room temperature for a ZnO thin film and VAN films with variable thickness (80, 160 and 250 nm). (b) Fitting of isotropic thermal models to the FDTR data. (c) Comparison of fitting isotropic and anisotropic thermal models to the FDTR data of a 160 nm thick VAN film.

results are shown of the fitting to an isotropic thermal conduction model, where only fitting parameter is  $k_2$ , i.e. the thermal conductivity along the film thickness. Although the fitting is not perfect, it provides reliable insights into the thermal conductivity behavior. The thermal conductivity of the ZnO reference film is determined to be  $38 \pm 5 \text{ W} \cdot \text{m}^{-1} \cdot \text{K}^{-1}$ , in good agreement with literature [9]. The (LSMO)<sub>0.1</sub>(ZnO)<sub>0.9</sub> VAN films show a strong reduction of the thermal conductivities, decreasing to  $12 \pm 2 \text{ W} \cdot \text{m}^{-1} \cdot \text{K}^{-1}$ ,  $9 \pm 2 \text{ W} \cdot \text{m}^{-1} \cdot \text{K}^{-1}$ , and  $8 \pm 2 \text{ W} \cdot \text{m}^{-1} \cdot \text{K}^{-1}$  for film thicknesses of respectively 250 nm, 160 nm, and 80 nm. The thermal conductivity is completely dominated by the nanopillar-matrix architecture, with the thickness being a small contribution to  $k_z$  in this range.

To investigate a possible anisotropy between in-plane and out-of-plane components of the thermal conductivity, the experimental data has been fitted using an anisotropic thermal conduction model. In the case of the ZnO reference film, including the thermal anisotropy in the model does not improve the fitting. For thicker VAN films (thickness of 250 nm) the anisotropy is also very small, with  $k_z = 12(2) \text{ W} \cdot \text{m}^{-1} \cdot \text{K}^{-1}$  and  $k_{xy} = 10(2) \text{ W} \cdot \text{m}^{-1} \cdot \text{K}^{-1}$ . On the other hand, including the anisotropy improves the fitting of the thinner films (VAN 160 nm), and suggests a much larger thermal anisotropy:  $\kappa_z = 9.2 \pm 2.0 \text{ W} \cdot \text{m}^{-1} \cdot \text{K}^{-1}$  and  $\kappa_{xy} = 1.5 \pm 0.5 \text{ W} \cdot \text{m}^{-1} \cdot \text{K}^{-1}$  (figure 10(c)). Note that the values of  $\kappa_z$  are similar to the ones obtained through fitting to the isotropic thermal model, indicating the robustness of the result.

# 4. Conclusion

VANs composed of self-assembled metallic La<sub>0.7</sub>Sr<sub>0.3</sub>MnO<sub>3</sub> (LSMO) nanopillars in a surrounding ZnO matrix are investigated for controllable thermal conductivity. The nanopillar-matrix architecture of the VAN films, with the introduction of small LSMO regions within a ZnO thin film, enhances the scattering of the phonons while enabling the easy transport of electrons. Tuning of the crystal orientation of the substrate controls the epitaxial alignment of the LSMO and ZnO phases along the horizontal and vertical interfaces. Highly ordered, crystalline LSMO:ZnO VAN films can be realized through self-assembly in which the epitaxial relation to the underlying substrate strongly affects the nanopillar-matrix architecture. The VAN films on (111)-oriented STO substrates exhibit a high Seebeck coefficient at 600 °C of about 980  $\mu$ V·K<sup>-1</sup>, typical for N-doped ZnO, in combination with an enhanced electrical conductivity due to the inclusion of LSMO nanopillars. This results in an increased power factor of 0.52  $\mu$ W·cm<sup>-1</sup>·K<sup>-2</sup> at 600 °C for the VAN film beyond the result for ZnO films of 0.15  $\mu$ W·cm<sup>-1</sup>·K<sup>-2</sup>. Detailed characterization of the thermal conductivity demonstrates a strong reduction, of nearly 75%, due to the nanostructure of the composite films. Also, signature of thermal anisotropy has been observed in the thinner VAN films, in strong contrast to the isotropic behavior in ZnO films. These results show the promising strategy of VAN thin films with a nanopillar-matrix architecture to scatter phonons and to enhance the thermoelectric performance.

#### Data availability statement

The data that support the findings of this study are openly available at the following URL/DOI: https://data.4tu.nl/.

# Acknowledgment

M W P and M H acknowledge funding through the Netherlands Organization for Scientific Research (NWO) under Perspective program 'ZERO: Towards Energy Autonomous Systems for IoT'(P15-06). Financial support was received from the European Union's Horizon 2020 research and innovation program under Grant Agreement No. 823717–ESTEEM3. A S acknowledges support from the Federal Ministry of Education and Research (Project NEUROTEC, Grants Nos. 16ME0398K and 16ME0399). F R acknowledges financial support from Ministerio de Ciencia (Spain), Project PID2022-138883NB-I00.

#### **ORCID** iDs

#### References

- [1] Win S L Y, Chiang Y-C, Huang T-L and Lai C-M 2024 Thermoelectric generator applications in buildings: a review *Sustainability* 16 7585
- [2] He J, Li K, Jia L, Zhu Y and Zhang H 2024 Advances in the applications of thermoelectric generators J. Linghu Appl. Therm. Eng. 236 121813
- [3] Shi X-L, Zou J and Chen Z-G 2020 Advanced thermoelectric design: from materials and structures to devices *Chem. Rev.* 120 7399–515
- [4] Wei J, Yang L, Ma Z, Song P, Zhang M, Ma J, Yang F and Wang X 2020 Review of current high-ZT thermoelectric materials *J. Mater. Sci.* 55 12642–704
- [5] d'Angelo M, Galassi C and Lecis N 2023 Thermoelectric materials and applications: a review Energies 16 6409
- [6] Ziman J M 1967 Electrons and Phonons. The Theory of Transport Phenomena in Solids (Clarendon Press)
- [7] Snyder G J and Toberer E S 2008 Complex thermoelectric materials Nat. Mater. 7 105-14
- [8] Christensen M, Abrahamsen A B, Christensen N B, Juranyi F, Andersen N H, Lefmann K, Andreasson J, Bahl C R H and Iversen B B 2008 Avoided crossing of rattler modes in thermoelectric materials Nat. Mater. 7 811–5
- [9] Tsubota T, Ohtaki M, Eguchi K and Arai H 1997 Thermoelectric properties of Al-doped ZnO as a promising oxide material for high-temperature thermoelectric conversion J. Mater. Chem. 7 85–90
- [10] Pei Y, Heinz N A, LaLonde A and Snyder G J 2011 Combination of large nanostructures and complex band structure for high performance thermoelectric lead telluride *Energy Environ. Sci.* 4 3640–5
- [11] Chen X, Zhou Z, Lin Y-H and Nan C 2020 Thermoelectric thin films: promising strategies and related mechanism on boosting energy conversion performance *J. Materiom.* 6 494–512
- [12] Chen R, Lee J, Lee W and Li D 2019 Thermoelectrics of nanowires Chem. Rev. 119 9260-302
- [13] Bourgeois O, Tainoff D, Tavakoli A, Liu Y, Blanc C, Boukhari M, Barski A and Hadji E 2016 Reduction of phonon mean free path: from low-temperature physics to room temperature applications in thermoelectricity C. R. Phys. 17 1154–60
- [14] Hicks L D and Dresselhaus M S 1993 Effect of quantum-well structures on the thermoelectric figure of merit Phys. Rev. B 47 12727–31
- [15] Hu C, Xia K, Fu C, Zhao X and Zhu T 2022 Carrier grain boundary scattering in thermoelectric materials *Energy Environ. Sci.* 15 1406–22
- [16] Biswas K, He J, Blum I D, Wu C-I, Hogan T P, Seidman D N, Dravid V P and Kanatzidis M G 2012 High-performance bulk thermoelectrics with all-scale hierarchical architectures Nature 489 414–8
- [17] MacManus-Driscoll J L, Zerrer P, Wang H, Yang H, Yoon J, Fouchet A, Yu R, Blamire M G and Jia Q 2008 Strain control and spontaneous phase ordering in vertical nanocomposite heteroepitaxial thin films Nat. Mater. 7 314–20
- [18] MacManus-Driscoll J L 2010 Self-assembled heteroepitaxial oxide nanocomposite thin film structures: designing interface-induced functionality in electronic materials Adv. Funct. Mater. 20 2035–45
- [19] Huang J, Li W, Yang H and MacManus-Driscoll J L 2021 Tailoring physical functionalities of complex oxides by vertically aligned nanocomposite thin-film design MRS Bull. 46 159–67
- [20] Chen A and Jia Q 2021 A pathway to desired functionalities in vertically aligned nanocomposites and related architectures MRS Bull. 46 115–22
- [21] Kang B S, Wang H, MacManus-Driscoll J L, Li Y, Jia Q X, Mihut I and Betts J B 2006 Low field magnetotransport properties of (La<sub>0.7</sub>Sr<sub>0.3</sub>MnO<sub>3</sub>)<sub>0.5</sub>:(ZnO)<sub>0.5</sub> nanocomposite films *Appl. Phys. Lett.* **88** 192514
- [22] Chen A, Bi Z, Tsai C-F, Lee J H, Su Q, Zhang X, Jia Q, MacManus-Driscoll J L and Wang H 2011 Tunable low-field magnetoresistance in (La<sub>0.7</sub>Sr<sub>0.3</sub>MnO<sub>3</sub>)<sub>0.5</sub>:(ZnO)<sub>0.5</sub> self-assembled vertically aligned nanocomposite thin films *Adv. Funct. Mater.* 21 2423–9
- [23] Zhang W R, Chen A P, Khatkhatay F, Tsai C F, Su Q, Jiao L, Zhang X H and Wang H Y 2013 Integration of self-assembled vertically aligned nanocomposite  $(La_{0.7}Sr_{0.3}MnO_3)_{(1-x)}$ : $(ZnO)_{(x)}$  thin films on silicon substrates ACS Appl. Mater. Interfaces 5 3995–9
- [24] Chen A, Zhang W, Khatkhatay F, Su Q, Tsai C-F, Chen L, Jia Q X, MacManus-Driscoll J L and Wang H 2013 Magnetotransport properties of quasi-one-dimensionally channeled vertically aligned heteroepitaxial nanomazes Appl. Phys. Lett. 102 093114
- [25] Navin K and Kurchania R 2018 Structural, magnetic and transport properties of the La<sub>0.7</sub>Sr<sub>0.3</sub>MnO<sub>3</sub>-ZnO nanocomposites J. Magn. Magn. Mater. 448 228–35
- [26] van de Putte M W, Polishchuk D, Gauquelin N, Verbeeck J, Koster G and Huijben M 2024 Control of magnetic shape anisotropy by nanopillar dimensionality in vertically aligned nanocomposites ACS Appl. Electron. Mater. 6 3695–703
- [27] Ohtaki M, Tsubota T, Eguchi K and Arai H 1996 High-temperature thermoelectric properties of (Zn<sub>1-x</sub>Al<sub>x</sub>)O J. Appl. Phys. 79 1816–8
- [28] Niu D L, Liu X J, Huang Q J and Zhang S Y 2005 Thermal diffusivity of La<sub>0.6</sub>Sr<sub>0.4</sub>MnO<sub>3</sub> thin film investigated by transient thermal grating technique *J. Phys. IV* **125** 249–51

- [29] Huijben M, Martin L W, Chu Y-H, Holcomb M B, Yu P, Rijnders G, Blank D H A and Ramesh R 2008 Critical thickness and orbital ordering in ultrathin La<sub>0.7</sub>Sr<sub>0.3</sub>MnO<sub>3</sub> films *Phys. Rev. B* 78 094413
- [30] Brinks P, Van Nong N, Pryds N, Rijnders G and Huijben M 2015 High-temperature stability of thermoelectric Ca<sub>3</sub>Co<sub>4</sub>O<sub>9</sub> thin films Appl. Phys. Lett. 106 143903
- [31] Varela-Domínguez N, Claro M S, Vázquez-Vázquez C, López-Quintela M A and Rivadulla F 2025 Electric-field control of the local thermal conductivity in charge transfer oxides *Adv. Mater.* 37 2413045
- [32] Schmidt A J, Cheaito R and Chiesa M 2009 A frequency-domain thermoreflectance method for the characterization of thermal properties Rev. Sci. Instrum. 80 094901
- [33] Langenberg E, Ferreiro-Vila E, Leborán V, Fumega A O, Pardo V and Rivadulla F 2016 Analysis of the temperature dependence of the thermal conductivity of insulating single crystal oxides *APL Mater.* 4 104815
- [34] Filonova E A, Demina A N, Kleibaum E A, Gavrilova L Y and Petrov A N 2006 Phase equilibria in the system LaMnO<sub>3+δ</sub>-SrMnO<sub>3</sub>-LaFeO<sub>3</sub>-SrFeO<sub>3-d</sub> Inorg. Mater. 42 443-7
- [35] Haynes W M, Lide D R and Bruno T J 2016 CRC Handbook of Chemistry and Physics (CRC Press)
- [36] Abramov Y A, Tsirelson V G, Zavodnik V E, Ivanov S A and Brown I D 1995 Acta Crystallogr. B 51 942
- [37] Wang L M, Lai J-H, Wu J I, Kuo Y-K and Chang C L 2007 Effects of Ru substitution for Mn on La<sub>0.7</sub>Sr<sub>0.3</sub>MnO<sub>3</sub> perovskites J. Appl. Phys. 102 023915
- [38] Hesselmann K, Knacke O and Kubaschewski O 1991 Thermochemical Properties of Inorganic Substances (Springer-Verlag)
- [39] Radaelli P G, Iannone G, Marezio M, Hwang H Y, Cheong S-W, Jorgensen J D and Argyriou D N 1997 Structural effects on the magnetic and transport properties of perovskite A<sub>1-x</sub>A'<sub>x</sub>MnO<sub>3</sub> (x=0.25, 0.30) *Phys. Rev. B* **56** 8265–76
- [40] Wang B et al 2013 Oxygen-driven anisotropic transport in ultra-thin manganite films Nat. Commun. 4 2778
- [41] Singh M and Singh M 2013 Thermal expansion in zinc oxide nanomaterials Nanosci. Nanotechnol. Res. 1 27-29
- [42] Meda L, Kennon L, Bacaltchuk C, Garmestani H and Dahmen K 2001 Effects of thermal annealing on the texture of La<sub>0.67</sub>Sr<sub>0.33</sub>MnO<sub>3</sub> thin films J. Mater. Res. 16 1887–9
- [43] Mukhin A, Ivanov V, Travkin V, Lebedev S, Pimenov A, Loidl A and Balbashov A 1998 Magnetic and structural transitions in La<sub>1-x</sub>Sr<sub>x</sub>MnO<sub>3</sub>: T-x phase diagram J. Exp. Theor. Phys. Lett. 68 356–62
- [44] Janotti A and Van de Walle C G 2009 Fundamentals of zinc oxide as a semiconductor Rep. Prog. Phys. 72 126501
- [45] Sikama P, Sararat C, Moontragoon P, Kaewmaraya T and Maensiri S 2018 Enhanced thermoelectric properties of N-doped ZnO and SrTiO<sub>3</sub>: a first principles study Appl. Surf. Sci. 446 47–58
- [46] Park C-S, Lee H-S, Shim D I, Cho H H, Park H-H and Kwon K-H 2016 The oxygen-deficiency-dependent Seebeck coefficient and electrical properties of mesoporous La<sub>0.7</sub>Sr<sub>0.3</sub>MnO<sub>3-x</sub> films *J. Mater. Chem. A* 4 4433–9
- [47] Park C S, Hong M-H, Shin S, Cho H H and Park H-H 2015 Synthesis of mesoporous La<sub>0.7</sub>Sr<sub>0.3</sub>MnO<sub>3</sub> thin films for thermoelectric materials J. Alloys Compd. 632 246–50
- [48] Van de Putte M W and Huijben M 2023 Epitaxial tin selenide thin film thermolectrics Appl. Surf. Sci. 623 157034
- [49] Wang X-K, Veremchuk I, Bobnar M, Zhao J-T and Grin Y 2016 Solid solution Pb<sub>1-x</sub>Eu<sub>x</sub>Te: constitution and thermoelectric behavior *Inorg. Chem. Front.* 3 1152–9
- [50] Zhai J, Wang H, Su W, Wang T, Mehmood F, Wang X, Chen T, Huo T, Zhang K and Wang C 2019 The p–n transformation and thermoelectric property optimization of  $Cu_{1+x}FeSe_2$  (x = 0-0.05) alloys J. Mater. Chem. C 7 9641–7
- [51] Maignan A, Martin C, Autret C, Hervieu M, Raveau B and Hejtmanek J 2002 Structural–magnetic phase diagram of Mo-substituted CaMnO<sub>3</sub>: consequences for thermoelectric power properties J. Mater. Chem. 12 1806–11
- [52] de Ligny D and Richet P 1996 High-temperature heat capacity and thermal expansion of SrTiO<sub>3</sub> and SrZrO<sub>3</sub> perovskites *Phys. Rev.* B 53 3013–22
- [53] Iwanaga H, Kunishige A and Takeuchi S 2000 Anisotropic thermal expansion in wurtzite-type crystals J. Mater. Sci. 35 2451-4
- [54] Cox S F J et al 2001 Experimental confirmation of the predicted shallow donor hydrogen state in zinc oxide *Phys. Rev. Lett.* 86 2601–04
- [55] Hofmann D M, Hofstaetter A, Leiter F, Zhou H, Henecker F, Meyer B K, Orlinskii S B, Schmidt J and Baranov P G 2002 Hydrogen: a relevant shallow donor in zinc oxide *Phys. Rev. Lett.* **88** 045504
- [56] Minegishi K, Koiwai Y, Kikuchi Y, Yano K, Kasuga M and Shimizu A 1997 Growth of p-type zinc oxide films by chemical vapor deposition Jpn. J. Appl. Phys. II 36 L1453
- [57] Look D C, Reynolds D C, Litton C W, Jones R L, Eason D B and Cantwell G 1830 Characterization of homoepitaxial p-type ZnO grown by molecular beam epitaxy *Appl. Phys. Lett.* 81 1830
- [58] Tsukazaki A *et al* 2005 Repeated temperature modulation epitaxy for p-type doping and light-emitting diode based on ZnO *Nat.*
- [59] Xia C, Qiao Z, Feng C, Kim J-S, Wang B and Zhu B 2018 Study on zinc oxide-based electrolytes in low-temperature solid oxide fuel cells *Materials* 11 40
- [60] Wilson R B, Apgar B A, Hsieh W-P, Martin L W and Cahill D G 2015 Thermal conductance of strongly bonded metal-oxide interfaces Phys. Rev. B 91 115414